WILEY-VCH

DOI: 10.1002/ ((please add manuscript number))
Article type: Full Paper

Title: Dependence of Photocurrent Enhancements in QD-Sensitized MoS_2 Devices on MoS_2 Film Properties

John J. Gough, Niall McEvoy, Maria O'Brien, Alan P. Bell, David McCloskey, John B. Boland,

*Jonathan N. Coleman, Georg S. Duesberg and A. Louise Bradley**

J. J. Gough, Prof. A. L. Bradley.
School of Physics and CRANN, Trinity College Dublin, College Green, Dublin 2, Ireland
E-mail: bradlel@tcd.ie

Dr. N. McEvoy, Dr. M. O'Brien, Dr. A. P. Bell, Prof. G. S. Duesberg.
School of Chemistry and CRANN, Trinity College Dublin, College Green, Dublin 2, Ireland.
AMBER Centre, Trinity College Dublin, College Green, Dublin 2, Ireland

Dr. D. McCloskey, J. B. Boland, Prof. J. N. Coleman.
School of Physics and CRANN, Trinity College Dublin, College Green, Dublin 2, Ireland.
AMBER Centre, Trinity College Dublin, College Green, Dublin 2, Ireland

Prof. G. S. Duesberg.
Institute of Physics, EIT 2, Faculty of Electrical Engineering and Information Technology, Universität der Bundeswehr München, Werner-Heisenberg-Weg 39, 85577 Neubiberg, Germany

Keywords: 2D materials, monolayers, quantum dots, photonics, electro-optical devices

Abstract

In this report we demonstrate highly efficient nonradiative energy transfer (NRET) from alloyed CdSeS/ZnS semiconductor nanocrystal quantum dots (QDs) to MoS_2 films of varying layer thicknesses, including pristine monolayers, mixed monolayer/bilayer, polycrystalline bilayers and bulk-like thicknesses, with NRET efficiencies of over 90%. Large-area MoS_2 films were grown on Si/SiO_2 substrates by chemical vapor deposition (CVD). Despite the ultrahigh NRET efficiencies there is no distinct increase in the MoS_2 photoluminescence intensity. However, by studying the optoelectronic properties of the MoS_2 devices before and after adding the QD sensitizing layer photocurrent enhancements as large as ~14 fold for pristine monolayer devices are observed, with enhancements on the order of ~2 fold for MoS_2 devices of mixed monolayer and bilayer thicknesses. For the polycrystalline bilayer and bulk-like MoS_2 devices there is almost no increase in the photocurrent after adding the QDs. Industrially scalable techniques were specifically utilised to fabricate the samples studied in this report, demonstrating the viability of this hybrid structure for commercial photodetector or light harvesting applications.

1. Introduction

Over the past decade there has been significant interest in two-dimensional (2D) materials. In particular, the transition metal dichalcogenide (TMDC) family of materials has been the subject of substantial investigation driven by their promising optical and electrical properties.[1–4] Much of this interest arises due to the fact that the layered material's electronic bandgap transitions from an indirect bandgap at a few-layer thickness to a direct bandgap at monolayer thickness.[1,3] The presence of a direct optical bandgap in the TMDC monolayers leads to promising applications in optoelectronic devices such as phototransistors[5–7] and photodetectors.[8] These devices are most commonly fabricated using few-layer and monolayer MoS_2 flakes obtained using mechanical exfoliation, a process that is not particularly scalable or reproducible. However, bottom-up approaches such as chemical vapor deposition (CVD) are

more desirable as these methods can achieve larger area coverage of monolayer and few-layer regions of the active material on the substrate.[9,10]

A significant drawback with these 2D materials is the low absorption of incident light as a result of the atomic thickness of the active region. This low absorption of incoming light limits the device in terms of both performance and efficiency. A common method used to increase the absorption of incoming light is to incorporate a sensitizing layer on top of the active region in the device. There have been a few reports of dye sensitized[11] and quantum dot (QD) sensitized[12,13] MoS_2 photodetectors in the literature. However, these demonstrations have focused on mechanically exfoliated MoS_2 devices and the mechanism for the transfer of energy from the sensitizing species was that of charge transfer. While charge transfer is an efficient energy transfer process, charge transfer has a stringent distance dependence (< 3 nm) and will only occur if the donor and acceptor wavefunctions overlap.[14] As mentioned, previous examples have used mechanical exfoliation techniques to obtain the monolayer material. This manuscript considers CVD-grown films of MoS_2 which provides large-area coverage of monolayer and mixed layer MoS_2 on the substrate; a quicker, cheaper and more suitable method for industrial processing.

Another method for the transfer of energy between donor and acceptor species is that of nonradiative energy transfer (NRET). NRET is an efficient dipole-dipole coupling mechanism which occurs due to the Coulomb interaction between confined excitons in the donor (QD) and acceptor (MoS_2) semiconducting species.[15,16] The efficiency of NRET relies on the spectral overlap between the donor emission and the acceptor absorption and the centre-to-centre distance between the donor and acceptor. Consideration of the dimensionality of the donor-acceptor pair (where the distance dependence of NRET is ultimately determined by the acceptor dimensionality[16]) and the electric field screening of the donor dipole in the acceptor medium are also important factors in the design of the optimal hybrid device.[16–18] NRET also has a well-defined distance dependence and can occur over distances of ~15 nm, beyond the limits

of charge transfer.[19,20] The NRET process has been reported for larger donor core-shell QDs in which the exciton is confined to the core.[18,21-24] The ability to control the aforementioned parameters makes the longer range NRET a promising mechanism applicable for applications in phototransistors,[25] photocells[26] and LEDs.[27]

Recent studies have demonstrated highly efficient NRET from semiconductor QDs to mono- and few-layer MoS_2.[15,21–24] It has been shown that the NRET efficiency increases as the number of layers of MoS_2 decreases, in contrast to the trend observed for NRET to graphene.[15] The increase in the NRET efficiency as the number of MoS_2 layers decreases is attributed to the reduced dielectric screening of the QD electric field in monolayer MoS_2.[15,22] QDs have many advantages as the donor species in such a hybrid system including tunable and narrow emission profiles, enhanced photostability, high quantum yield and broadband optical absorption which allows for a broad range of excitation wavelengths, in contrast with organic dyes.[28,29]

CVD growth techniques are the proposed route towards large-scale synthesis of monolayer MoS_2. However, while the process results in large-area growth of MoS_2 on the substrate it does not specifically yield purely monolayer material across the entire area. There are regions of monolayer, mixed layer, polycrystalline, and bulk-like thicknesses of MoS_2 on the substrate. In this study, we address how the performance of the hybrid QD-MoS_2 devices varies as the MoS_2 channels gradually change from pristine monolayers to more polycrystalline channels. The degree of crystallinity of the MoS_2 channels was identified using Raman and photoluminescence (PL) mapping and the MoS_2 layer thicknesses were determined using Raman spectroscopy. We find the largest photocurrent enhancements for the pristine monolayer devices, after the addition of the QDs, and little to no enhancement for the polycrystalline devices. This indicates that the NRET from the QDs has less impact on the extracted photocurrent of polycrystalline samples.

2. Results and Discussion

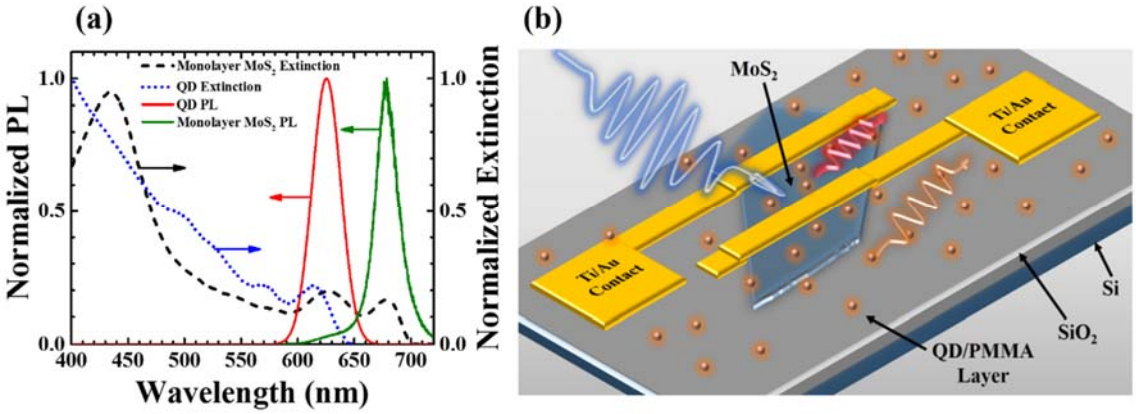

Figure 1. (a) Extinction spectra of monolayer MoS_2 (black dash) and QDs in PMMA (blue dot), and normalized PL spectra of monolayer MoS_2 (green solid) and QDs in PMMA (red solid). The PL spectra were acquired under excitation with a 405 nm pulsed laser diode. The extinction spectrum of monolayer MoS_2 was measured from a CVD-grown triangular monolayer on a quartz substrate. The extinction spectrum of the QDs was obtained from the solution of QDs in PMMA that was subsequently spincast onto the devices. (b) Schematic diagram of experimental device.

The optical characteristics of monolayer MoS_2 and QDs in 0.1% wt. PMMA are shown in **Figure 1**a. The alloyed CdSeS/ZnS QDs, with a diameter of (6.0 ± 0.7) nm (see Figure S1 in the Supporting Information), have a peak emission wavelength of 630 nm which overlaps well with the B exciton of the monolayer MoS_2 at ~ 630 nm. The monolayer MoS_2 has a peak emission wavelength of ~ 677 nm corresponding with the spectral position of the A exciton. A schematic representation of the experimental devices is shown in Figure 1b. The hybrid devices are realized by spin coating a dilute monolayer of QDs in PMMA on top of the chip containing the devices with a concentration of ~ 2.3 x10^{11} QDs/m^2. Spectral and time-resolved PL (TRPL) measurements are compared on and off the MoS_2 film on the same chip. Strong quenching of the QD emission and a faster QD PL decay are observed on the film indicating the introduction of a new relaxation mechanism. The quenching is attributed to NRET, as found in previously

reported experiments, due to the larger size of core-shell QDs, ligand, dispersion in the PMMA host, confinement of the exciton to the QD core and strong overlap of the QD emission with the B exciton peak of the MoS_2 absorption spectrum.[18,21-24] The measured NRET efficiency, η_{NRET}, of over 90% (see Figure S2 in the Supporting Information) is also consistent with values reported in the literature.[22,23] Despite the large NRET efficiency no appreciable increase in the MoS_2 PL intensity is observed (See Figure S2 in the Supporting Information), which is thought to be due to nonradiative recombination at defect sites in the MoS_2. Observation of increased PL emission from the acceptor (MoS_2) resulting from NRET relies on the radiative recombination of excitons. However, the electrical processes depend more on the separation of the photo-generated charge carriers under an applied bias. Therefore, it is of interest to investigate the electrical extraction of energy transferred from the donor to the acceptor by NRET.

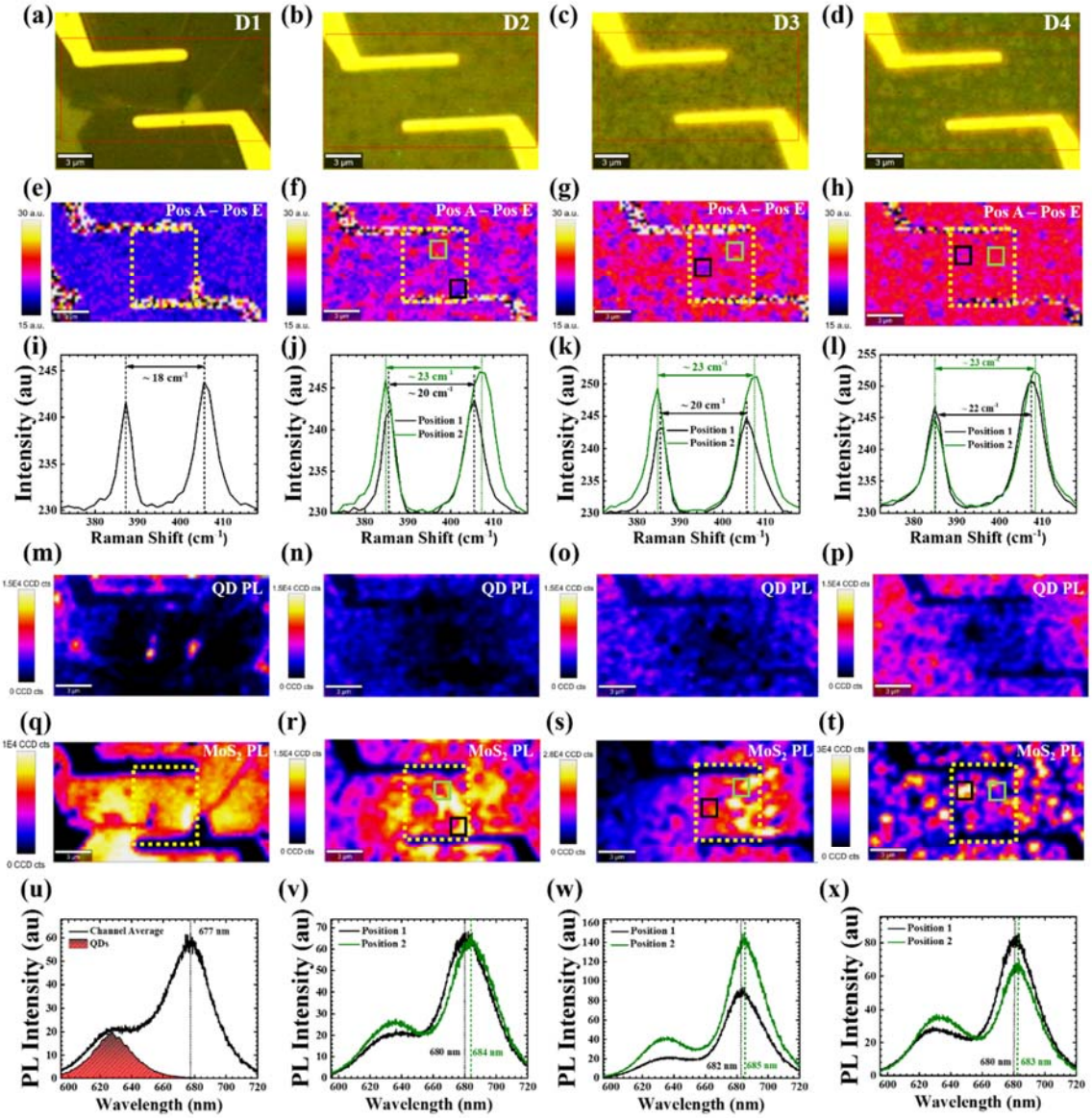

Figure 2. (a-d) Optical images of MoS_2 devices (red boxes indicate the PL and Raman mapping areas). (e-h) Raman maps indicating the separation between the *A* and *E* peak positions. The yellow dash box represents the channel in the devices. Black and green boxes correspond to the regions where the Raman and PL spectra were extracted, shown in (i-l) and (u-x), respectively. (m-p) PL maps of the same areas highlighted in the red boxes in the optical images (a-d).The PL maps are centered on the QD peak emission wavelength (630 nm). The maps clearly show that the QD emission is quenched most strongly on the monolayer device and less quenched moving to the right. (q-t) PL maps of the devices centered on the MoS_2 peak emission wavelength. (u-x) PL spectra extracted from the maps in areas indicated by black and green

boxes on the Raman maps in (f-h). The QD PL spectrum, measured from a position on the sample containing no MoS_2, is shown in (u) to indicate the peak position of the QDs relative to the MoS_2 B emission peak. There is a clear redshift in the MoS_2 peak emission wavelength as the MoS_2 thickness increases from monolayer to bilayer. The regions where there are a change in layer thickness are indicated by black and green boxes in the Raman maps and represented by the corresponding colors in the Raman and PL spectra in (i-l) and (u-x), respectively. Higher QD PL emission is observed on the regions of increased layer thicknesses, indicating a reduction in the NRET efficiency. The NRET efficiency is highest on the monolayer MoS_2. A full set of data for a bulk-like device is shown in Figure S3 (Supporting Information).

Optical images of four devices (D1, D2, D3 and D4) are shown in **Figure 2**a-d. The volume of bilayer MoS_2 is increasing across the devices, moving from a purely pristine monolayer device, D1 (Figure 2a), to a polycrystalline bilayer device, D4 (Figure 2d). The devices, D2 and D3 (Figure 2, panels b and c, respectively), are representative of intermediary phases between pristine monolayer and polycrystalline bilayer. The assignment of the sample crystallinity is discussed in detail below. The red box in each device image (Figure 2, panels a-d) indicates the region in which Raman and PL mapping was performed. It is clear from the optical images that the polycrystallinity of the devices is increasing from D1 to D4, with D1 showing a pristine and uniform channel area while D4 appears to have a multitude of nucleation points throughout the channel and a clear abundance of bilayer MoS_2. It is also worth noting that device, D3 (Figure 2c), has more bilayer regions in the channel than device, D2 (Figure 2b). Raman maps of the areas indicated by red boxes in Figure 2, panels a-d, are presented in Figure 2, panels e-h, respectively. These Raman maps plot the separation between the *A* and *E* peak positions in the MoS_2 Raman spectrum. Device D1 (Figure 2e) shows no variation in the peak position across the device, indicating the presence of a uniform and pristine layer. The corresponding Raman spectrum averaged over the region indicated by a dash yellow box (excluding the electrodes) in

Figure 2e is given in Figure 2i, showing a separation between the *A* and *E* peaks of ~18 cm^{-1}, which is consistent with the presence of monolayer MoS_2.[30,31] The Raman maps in Figure 2, panels f and g, indicate the emergence of nucleation points of bilayer thicknesses through an increased separation between the *A* and *E* peaks.[30,31] The Raman spectra in Figure 2, panels j and k, are taken from the regions identified by black and green squares in Figure 2, panels f and g, respectively. The black and green line spectra are measured in the areas indicated by black and green squares, respectively. The regions indicated in black and green on both devices in Figure 2, panels f and g, show a separation between the *A* and *E* peaks of ~20 cm^{-1} and ~23 cm^{-1}, respectively, indicating the presence of both monolayer and bilayer MoS_2.[30,31] The slight increase in the separation between the *A* and *E* peaks on the monolayer regions from 18 cm^{-1} on the purely monolayer device, D1 (Figure 2i), to a separation of 20 cm^{-1} on the devices containing a mixture of both monolayer and bilayer MoS_2, D2 and D3 (Figure 2, panels j and k), is attributed to signal mixing due to the small size of the grains on the devices, with similar effects observed in the corresponding PL spectra (Figure 2, panels u-w). It should be noted that while both devices, D2 and D3, contain a mixture of monolayer and bilayer MoS_2, there is a larger proportion of bilayer MoS_2 in the channel of the device D3 (Figure 2g) as compared to device D2 (Figure 2f). The Raman map for device D4 (Figure 2h) again shows little variation in the separation between the *A* and *E* peaks. The corresponding Raman spectra (Figure 2l) reveal separations of ~22 cm^{-1} and ~23 cm^{-1} indicating that the majority of MoS_2 in the device channel is of bilayer thickness.[30,31] The channel in the bulk-like device presented in Figure S3 (Supporting Information) consists mainly of bulk thicknesses with a separation between the *A* and *E* Raman peaks of ~25 cm^{-1}, with a small region of bilayer thickness, having a separation between the *A* and *E* Raman peaks of ~22 cm^{-1}.

PL mapping was also carried out on each of the devices following the addition of the QD sensitizing layer. These PL maps help not only to identify the MoS_2 emission intensity and peak

wavelength but they can also reveal information regarding the interaction between the QDs and the MoS_2, such as quenching of the QD PL which is indicative of NRET. The QD PL maps for each device can be seen in Figure 2, panels m-p. The PL maps are centered on the QD peak emission wavelength (630 nm) to indicate the relative PL intensity on each of the devices. It is instantly apparent that the strongest quenching of the QD emission occurs on the monolayer device, D1 (Figure 2m). Quenching of the QD emission decreases moving from devices D2 to D4, as the devices become more polycrystalline with the nucleation of bilayer regions (Figure 2, panels n-p). This indicates that the NRET efficiency decreases as the MoS_2 layer number increases, which is consistent with optical studies in the literature.[15,22] From the QD PL maps for the devices D2 and D3 (Figure 2, panels n and o) the quenching of the QD PL is strongest in the monolayer regions that can be seen in the corresponding Raman maps (Figure 2, panels f and g), respectively, further confirming the decrease in NRET efficiency as the MoS_2 layer number increases. There is a much weaker quenching of the QD PL on the polycrystalline bilayer device, D4, as can be seen from the PL map (Figure 2p), which is expected due to increased dielectric screening of the QD electric field dipole in the bilayer material, in contrast to the monolayer material.[15,22]

PL maps of the devices, centered on the MoS_2 peak emission wavelength are presented in Figure 2, panels q-t. These PL maps clearly demonstrate that the regions of high PL intensity are decreasing as the devices transition from pristine monolayer (D1) to polycrystalline bilayer (D4). The MoS_2 PL intensity is fairly uniform across the monolayer device, D1 (Figure 2q), while the PL is quite non-uniform across devices D2 to D4 and the areas showing high PL intensity are reducing (Figure 2, panels r, s and t, respectively). While the Raman maps indicate the regions of the device that differ in layer thickness, the corresponding MoS_2 PL maps do not show similar patterns in terms of the PL intensity. The PL maps reveal that for devices D2 and D3 (Figure 2, panels r and s) the PL intensity is larger in regions where there is variation of

layer number as can be seen in the corresponding Raman maps (Figure 2, panels f and g) and not solely higher PL intensity from monolayer regions as is expected. The corresponding PL spectra for each of the PL maps are shown in Figure 2, panels u-x. Similar to the Raman spectrum in Figure 2i, the PL spectrum in Figure 2u is an average over the device channel indicated by the yellow dash box in Figure 2e. The pristine monolayer MoS_2 has a peak emission wavelength of ~ 677 nm which is expected for monolayer MoS_2 flakes.[3] The QD PL spectrum is also shown in Figure 2u to indicate the peak position relative to the MoS_2 B emission peak. The black and green lines in the PL spectra in Figure 2, panels v-x, were extracted from the same regions as the Raman spectra in Figure 2. The PL spectra in Figure 2, panels v and w, show both a redshift in the peak emission wavelength for MoS_2 and an increase in QD PL intensity at the bilayer thickness locations, as expected. However, both devices consisting of a mix of monolayer and bilayer MoS_2 show PL intensities for the bilayer region either equal to or greater than the PL intensity from the purely monolayer region. This increase in PL intensity can be attributed to increased scattering at defect sites introduced by the grain boundaries[32] at the edges of the nucleation sites where the second layer has formed. The PL spectra for the polycrystalline bilayer device, D4 (Figure 2t), shows a larger QD PL intensity as compared to the other devices and shows very little variation in the MoS_2 PL intensity across the whole device, once again verifying the decrease in the NRET efficiency. Similarly, the bulk-like device presented in Figure S3 (Supporting Information) shows higher QD PL intensities and lower MoS_2 PL intensities as compared with the devices presented in the main manuscript (D1-D4), indicating a lower NRET efficiency from the QDs to the bulk-like MoS_2 and reduced emission intensity from the bulk-like material.

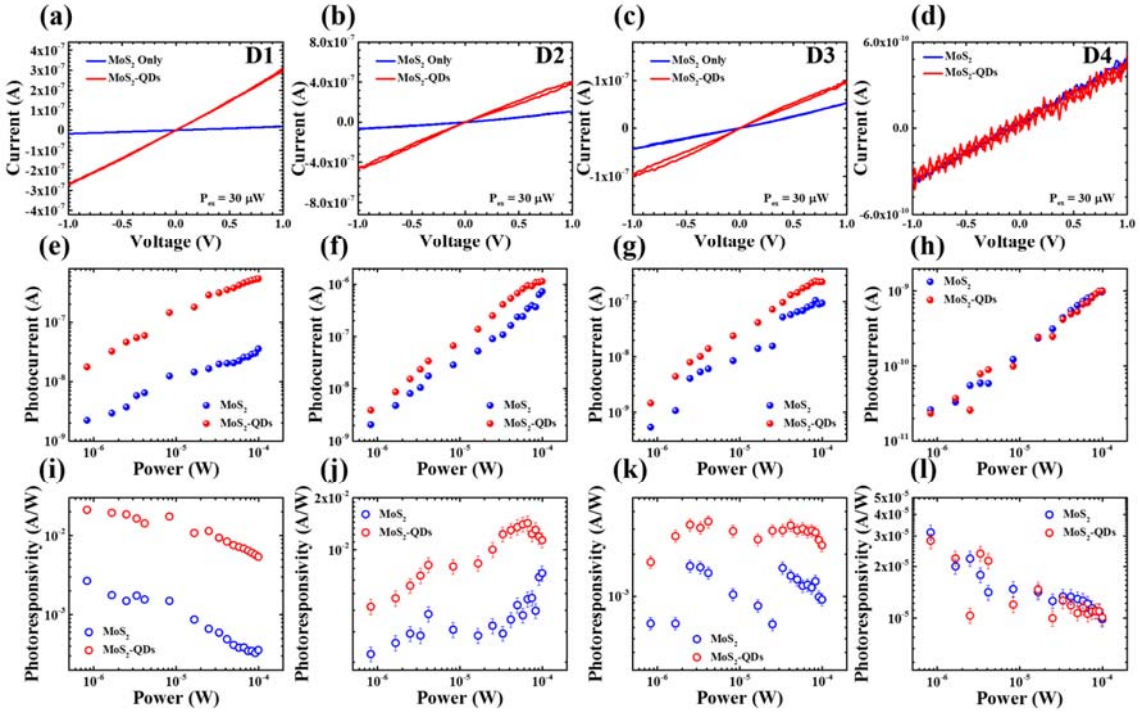

Figure 3. (a-d) I-V curves for the MoS_2 devices before (blue line) and after the addition of the QD sensitizing layer (red line). The I-V curves were measured under excitation from a 405 nm laser at an excitation power of 30 μW. (e-h) Plots of photocurrent as a function of excitation power for each MoS_2 device before (blue dots) and after the addition of the QD sensitizing layer (red dots). (i-l) Photoresponsivity of each device before (blue open circles) and after the addition of the QD sensitizing layer (red open circles).

The current-voltage (I-V) characteristics for each device (before and after the addition of the QD sensitizing layer) were measured as a function of laser excitation power in the range of ~1-100 μW between -1 and +1 V. All devices were measured under the same conditions and had a linear or close to linear I-V curve at all laser powers before and after the addition of the QD sensitizing layer. I-V curves for each device at a laser excitation power of 30 μW with (red) and without (blue) the QD sensitizing layer are shown in **Figure 3**, panels a-d. The largest enhancement in photocurrent is seen for the pristine monolayer device, D1 (Figure 3a). Similar enhancements are observed for devices D2 and D3, both containing portions of monolayer and

bilayer MoS_2 (Figure 3, panels b and c). There is little to no enhancement of the photocurrent for the polycrystalline bilayer device, D4, shown in Figure 3d. The bulk-like device also shows no enhancement in the photocurrent following the addition of the QD sensitizing layer (See Figure S3 in Supporting Information).

Figure 3, panel e-h, show the generated photocurrent, I_{Ph}, as a function of laser excitation power for the four devices. All devices exhibit a similar dependence on the excitation power before and after the addition of the QD sensitizing layer, having either a linear or slightly sub/super-linear slope. Similar to the I-V curves (Figure 3, panels a-d) it is clear that the largest enhancement in the photocurrent is obtained from the purely monolayer device, D1 (Figure 3e), with comparable levels of photocurrent enhancement across the full excitation power range for the devices D2 and D3, containing regions of both monolayer and bilayer MoS_2 (Figure 3, panels f and g). It is worth pointing out that while the device, D3, containing more bilayer than monolayer regions (Figure 2c) should give higher levels of photocurrent due to a greater abundance of charge carriers, we observe lower levels of photocurrent compared to device, D2, which contains almost equal portions of monolayer and bilayer regions (Figure 2b). We attribute this to a larger number of grain boundaries in the channel leading to a larger density of scattering points (Figure 2c), this is also in agreement with the PL from the bilayer regions shown in Figure 2w. The photocurrent obtained from the polycrystalline bilayer device, D4 (Figure 3h), shows almost identical curves with and without the QD sensitizing layer indicating that the addition of the sensitizing layer has no effect on polycrystalline bilayer devices resulting from a combination of grain boundaries leading to electron scattering at defect points, and increased dielectric screening of the QD electric field dipole in the bilayer material.[15,22] Measurements performed on the bulk-like device also reveal is no enhancement of the photocurrent after the addition of the QD sensitizing layer (See Figure S3 in Supporting Information).

The photoresponsivity, R, gives a measure of the current output as a function of incident optical power. The photoresponsivity is given by $R = I_{Ph}/P_{ex}$, where P_{ex} is the excitation power. The photoresponsivity measured for each of the devices across the full excitation power range is given in Figure 3, panels i-l. The photoresponsivity of the pristine monolayer device, D1 (Figure 3i), shows a typically steady decrease in photoresponsivity as the optical excitation power increases which corresponds to a sub-linear dependence of photocurrent on the excitation power. The largest photoresponsivity for the monolayer device is achieved at the lowest excitation power of ~1 μW for both the MoS_2 device only (R = 2.6 x10^{-3} A/W) and with the QD sensitizing layer (R = 2.1 x10^{-2} A/W), giving > 8 fold enhancement in photoresponsivity. The photoresponsivity curves for the mixed layer devices, D2 and D3 (Figure 3, panels j and l, respectively) however, display a different character as compared to the monolayer device, D1. These devices show a combination of increasing, constant and decreasing photoresponsivity regimes as the excitation power increases. The increasing and constant regimes correspond to super-linear and linear dependences of photocurrent on excitation power, respectively. Sub-linear dependence of photocurrent on excitation power in MoS_2 devices is commonly observed at large excitation intensity[8,33,34] while linear dependences are observed at lower excitation intensities.[5,7,8] However, a super-linear dependence of the photocurrent on excitation power is less documented and can be explained by multi-centre recombination models.[35] The presence of surface defects and edge states at grain boundaries, due to the granular nature of the channel in devices D2 and D3, could give rise to a variety of recombination centers, such as dangling bonds at the MoS_2 surface, and contribute to this super-linear behavior.[35–39] Device D4 shows a similar decrease in the photoresponsivity with increasing excitation power as for D1 both with and without the QD sensitizing layer.

To calculate the average photocurrent enhancement for each of the devices, the photocurrent *vs.* excitation power curves were averaged across the full laser excitation power range. The enhancement was then calculated as $I_{MoS2\text{-}QDs}/I_{MoS2}$. We find photocurrent enhancements as high

as ~14 fold for the pristine monolayer device and photocurrent enhancements of ~2 fold for devices D2 and D3, and no enhancement for device D4 after adding the QD sensitizing layer (**Figure 4**a). There is also no enhancement for the bulk-like device presented in Figure S3 (Supporting Information). This indicates that the QD sensitizing layer is most effective for monolayer devices, while the benefits of the QD sensitizing layer disappear as the MoS_2 regions in the device become polycrystalline.

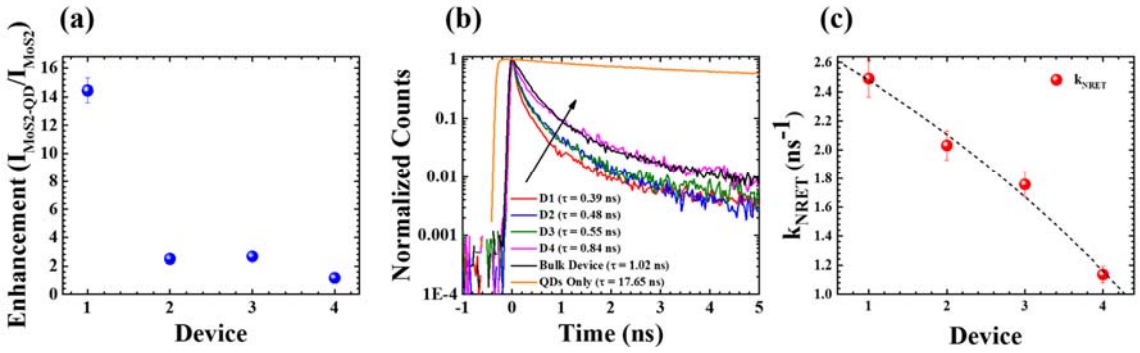

Figure 4. (a) Average photocurrent enhancement for each device. (b) PL decay curves of the QDs off the MoS_2 (orange) and the QDs on each of the devices. The decays are presented over the first 5 ns for easier comparison of the curves. Full decays are presented in the supporting information, Figure S4. (c) NRET rate between the QDs and MoS_2 in each of the devices. The black dash line in c is a guide to the eye.

Time-resolved PL (TRPL) measurements were performed to further investigate the interaction between the QDs and the MoS_2 devices. The PL decay curves for the QDs off the MoS_2 and on each of the devices are presented in Figure 4b. The PL decays were fit with a bi-exponential decay curve given by

$$I(t) = I_1 e^{-\frac{t}{\tau_1}} + I_2 e^{-\frac{t}{\tau_2}} \quad (1)$$

where I_1 and I_2 are the intensities of both decays with lifetimes of τ_1 and τ_2, respectively. The average lifetime was calculated from the fitting parameters as an intensity weighted average lifetime, τ_{Avg}, given by

$$\tau_{Avg} = \frac{I_1\tau_1^2 + I_2\tau_2^2}{I_1\tau_1 + I_2\tau_2} \quad (2)$$

The QD PL lifetime measured off the MoS_2 film represents the total spontaneous emission lifetime, $\tau_{QD} = k_r^{-1} + k_{nr}^{-1}$, where k_r and k_{nr} are the radiative and nonradiative decay rates, respectively, and therefore the lifetime takes account of the intrinsic QD carrier dynamics in a dilute monolayer on the chip. The total PL lifetime of the QDs on the MoS_2 is $\tau_{QD-MoS_2} = k_r^{-1} + k_{nr}^{-1} + k_{NRET}^{-1}$, where k_r and k_{nr} are the same as the QD reference off the MoS_2 and k_{NRET} is the rate of NRET from the QDs to the MoS_2. Therefore, $k_{NRET} = \tau_{QD-MoS_2}^{-1} - \tau_{QD}^{-1}$ and the NRET efficiency is given by $\eta_{NRET} = \frac{k_{NRET}}{k_r + k_{nr} + k_{NRET}} = 1 - \frac{\tau_{QD-MoS_2}}{\tau_{QD}}$. The substantial reduction in the QD PL lifetime on the MoS_2 devices indicates that the NRET process is highly efficient in this hybrid system, with NRET efficiencies, η_{NRET}, of over 90% for each of the devices including the bulk-like thickness device (See Figure S4 in the Supporting information). The highest NRET efficiency is found for the pristine monolayer device, D1, with an NRET efficiency of ~98 ± 3%, while the TRPL measurements on the more polycrystalline devices, D2, D3 and D4, reveal NRET efficiencies of ~97 ± 2%, ~97 ± 3% and 95 ± 2%, respectively. The NRET efficiency for the bulk-like thickness device is ~94 ± 2%.

The NRET rate, k_{NRET}, provides further information on the temporal scale over which the NRET process occurs. A plot of the NRET rates for each device is presented in Figure 4c. There is a clear trend in the reduction of the NRET rate as the devices become more polycrystalline. The NRET rate between the QDs and the polycrystalline bilayer device, D4, is ~1.1 ± 0.1 ns^{-1} which is less than half the NRET rate between the QDs and the monolayer device, D1, which has an NRET rate of ~2.5 ± 0.1 ns^{-1}. This increase in the NRET rate as the devices reach monolayer thickness is due to the reduced dielectric screening of external electric fields in the MoS_2 as the layer number decreases.[15,22] The difference in NRET across the devices cannot account for the larger difference in the photocurrent enhancement. The larger variation in the

photocurrent enhancement can be explained by the increased number of grain boundaries arising from the formation of bilayer MoS_2 at nucleation points leading to greater scattering of electrons[40–42] and consequently reduced mobility. This lower enhancement resulting from poor carrier transport due to the scattering of electrons is consistent with the photocurrent and photoresponsivity values obtained from the devices as they become more polycrystalline in Figure 3, panels b-d, and f-h, respectively. Typically, as the proportion of bilayer MoS_2 increases an increase in photocurrent could be expected due to the larger number of charge carriers available[1,33,43]. However, the observed decrease in device performance is due to the increasing number of grain boundaries and defect sites.

3. Conclusion

In summary the optoelectronic properties of hybrid QD-MoS_2 devices show a strong dependence on the properties of the MoS_2 layer, despite highly efficient NRET from semiconductor QDs in an ultrathin sensitizing layer to a variety of MoS_2 devices varying from pristine monolayer to polycrystalline devices composed of mixed layer thicknesses (monolayer and bilayer). While NRET efficiencies exceeding 90% have been demonstrated across all devices, measurements reveal a decrease in the NRET efficiency and rate as the ratio of bilayer to monolayer MoS_2 in the device channels increases. Despite the high NRET efficiency, spectral PL measurements reveal that there is little to no enhancement of the MoS_2 PL intensity after the addition of the QD sensitizing layer, attributed to nonradiative recombination of excitons at defect sites. Optoelectronic measurements revealed that the energy transferred from the QDs to the MoS_2 through NRET pathways could be extracted electrically. Photocurrent enhancements as large as ~14 fold were found for the pristine monolayer MoS_2 device after adding the QD sensitizing layer, while devices consisting of a mixture of monolayer and bilayer MoS_2 gave ~2 fold enhancement. No enhancement was observed as the active region of the devices became more polycrystalline and predominantly bilayer. The photocurrent

measurements also revealed that the photocurrent decreased as the devices became more polycrystalline due to increased scattering of charge carriers, and lower photocurrent enhancements were observed. Importantly, we have demonstrated that increased absorption of incident light in a 2D photodetection system can enhance the electrical output from the 2D material using NRET, with the greatest advantages obtained from monolayer MoS_2 devices. This hybrid system which combines large-area synthesis of MoS_2 films and a simple spin-coating process, both of which are industrially scalable and economically viable methods, suggests a potential route for hybrid 2D optoelectronic devices, most notably, photodetection and light harvesting applications.

4. Experimental Section

Growth of MoS_2: Large-area coverage of MoS_2 was achieved using a previously reported CVD growth technique.[10] In brief, a microreactor was formed between the seed and target substrates by placing a target substrate (typically a blank SiO_2/Si substrate) face down on top of a seed substrate, which consisted of liquid-phase exfoliated MoO_3 nanosheets[44] drop cast onto a Si/SiO_2 substrate. This microreactor was placed into the center of a quartz tube furnace where it was heated to 750 ºC under 150 sccm Ar flow and then exposed to sulfur vapor, which was generated by heating sulfur powder to ~120 ºC in an independently-controlled upstream zone of the furnace. While this technique produces MoS_2 which is predominantly monolayer, regions of other layer thickness could be identified by optical inspection of the substrates.

Preparation of QD/PMMA layers: Alloyed CdSeS/ZnS QDs (1 mg/mL) in toluene were purchased from Sigma-Aldrich. The QDs were used as supplied in stock solution. The QD/PMMA solutions were made up by dispersing the stock QDs (12.5 µL) in 0.1% wt. PMMA in toluene (500 µL). The dispersions were sonicated for 20 s to ensure even dispersion of the QDs (diameter = 6.0 ± 0.7 nm) in the PMMA solution.

Extinction Measurement of Monolayer MoS_2: The extinction spectrum of the monolayer MoS_2 was measured following the CVD of MoS_2 onto a quartz substrate. The extinction measurement was then performed using a custom built transmission apparatus using a Xenon lamp and a 100x microscope objective.

MoS_2 Characterization: The CVD-grown MoS_2 used in this study was characterized by photoluminescence (PL) and Raman spectroscopy. These measurements were performed using a WITec Alpha 300R tool with a 532 nm excitation laser operating at a power of ~250 μW with a 100x objective (N.A. = 0.95). Maps were obtained by acquiring 4 spectra per μm in x and y directions. For PL measurements a spectral grating with 600 lines/mm was used whereas for Raman measurements a higher-resolution spectral grating with 1800 lines/mm was used.

Time-resolved Photoluminescence: Time-resolved photoluminescence (TRPL) measurements were performed using a PicoQuant Microtime200 time-resolved confocal microscope system using an excitation of 90 ps pulses at a wavelength of 405 nm with a repetition rate of 10 MHz and an integration time of 4 ms per pixel. The laser spot size was ~430 nm. The sample was excited through a 40x objective (NA = 0.65) and the PL was collected through the same objective. The excitation power used for the measurements was 1.0 μW. All scans were performed over 3 μm x 3 μm square areas in the device channels (excluding the QD only measurements). A bandpass filter, centered at 635 nm and with a 10 nm full-width-at-half-maximum, was used to ensure that only the PL from the QDs was collected.

Device Fabrication: The electrical devices were fabricated by patterning a PMMA resist using electron beam lithography (EBL). The Ti/Au (5 nm/ 45 nm) contact pads and electrodes were deposited using electron beam evaporation. The contact pads have dimensions of 80 μm x 80 μm and each device has a 5 μm channel length between the electrodes. All MoS_2 devices discussed in this manuscript were grown on the same Si/SiO_2 chip in a single growth process, these devices were also patterned in a single EBL run.

The hybrid devices were realized by spin casting an ultra-thin layer (~8 nm, See Figure S5 in the Supporting Information) of dilute QDs in 0.1% wt. PMMA (12.5 µL QDs in 500 µL PMMA) to achieve monolayer coverage of QDs on the MoS_2 devices. The MoS_2 samples were characterized using scanning Raman spectroscopy to obtain a map of the active region in the devices and identify the number of MoS_2 layers[30] in the channel. As a result of the large (5 µm) channel length for each of the devices we find very little current during dark measurements. However this large channel length was necessary to ensure that the laser excitation spot (~3 µm diameter) could fit comfortably in the centre of the channel without impinging on the electrodes. The excitation laser used for the photocurrent measurements was a variable power Toptica iBeam smart laser diode with a 405 nm excitation wavelength. The active regions of the devices were excited through a 10x objective (NA = 0.25) with an excitation spot diameter of ~ 3µm. The electrical measurements were carried out using a Keithley 2400 source meter to provide a bias and measure the current through the devices.

Supporting Information

Supporting Information is available from the Wiley Online Library or from the author.

Acknowledgements

We thank Eoin McCarthy for the TEM measurements of the quantum dots. This work was supported by Science Foundation Ireland (SFI) under grant numbers 10/IN.1/12975, 15/IA/3131 and 15/SIRG/3329. JJG acknowledges a postgraduate research scholarship from the Irish Research Council (IRC) GOIPG/2013/680. MO'B acknowledges a postgraduate research scholarship from the Irish Research Council (IRC) via the Enterprise Partnership Scheme, Project 201517, Award number 12508.

Received: ((will be filled in by the editorial staff))
Revised: ((will be filled in by the editorial staff))
Published online: ((will be filled in by the editorial staff))

References

[1] K. F. Mak, C. Lee, J. Hone, J. Shan, T. F. Heinz, *Phys. Rev. Lett.* **2010**, *105*, 136805.

[2] G. Eda, H. Yamaguchi, D. Voiry, T. Fujita, M. Chen, M. Chhowalla, *Nano Lett.* **2011**, *11*, 5111.

[3] A. Splendiani, L. Sun, Y. Zhang, T. Li, J. Kim, C.-Y. Chim, G. Galli, F. Wang, *Nano Lett.* **2010**, *10*, 1271.

[4] B. Radisavljevic, A. Radenovic, J. Brivio, V. Giacometti, A. Kis, *Nat. Nanotechnol.* **2011**, *6*, 147.

[5] Z. Yin, H. Li, H. Li, L. Jiang, Y. Shi, Y. Sun, G. Lu, Q. Zhang, X. Chen, H. Zhang, *ACS Nano* **2012**, *6*, 74.

[6] H. S. Lee, S. Min, Y. Chang, M. K. Park, T. Nam, H. Kim, J. H. Kim, S. Ryu, S. Im, *Nano Lett.* **2012**, *12*, 3695.

[7] W. Zhang, J.-K. Huang, C.-H. Chen, Y.-H. Chang, Y.-J. Cheng, L.-J. Li, *Adv. Mater.* **2013**, *25*, 3456.

[8] O. Lopez-Sanchez, D. Lembke, M. Kayci, A. Radenovic, A. Kis, *Nat. Nanotechnol.* **2013**, *8*, 497.

[9] J. Mann, D. Sun, Q. Ma, J. R. Chen, E. Preciado, T. Ohta, B. Diaconescu, K. Yamaguchi, T. Tran, M. Wurch, K. Magnone, T. F. Heinz, G. L. Kellogg, R. Kawakami, L. Bartels, *Eur. Phys. J. B* **2013**, *86*, 2.

[10] M. O'Brien, N. McEvoy, T. Hallam, H.-Y. Kim, N. C. Berner, D. Hanlon, K. Lee, J. N. Coleman, G. S. Duesberg, *Sci. Rep.* **2014**, *4*, 7374.

[11] S. H. Yu, Y. Lee, S. K. Jang, J. Kang, J. Jeon, C. Lee, J. Y. Lee, H. Kim, E. Hwang, S. Lee, J. H. Cho, *ACS Nano* **2014**, *8*, 8285.

[12] D. Kufer, I. Nikitskiy, T. Lasanta, G. Navickaite, F. H. L. Koppens, G. Konstantatos, *Adv. Mater.* **2015**, *27*, 176.

[13] D. Kufer, T. Lasanta, M. Bernechea, F. H. L. Koppens, G. Konstantatos, *ACS Photonics* **2016**, *3*, 1324.

[14] D. L. Dexter, *J. Chem. Phys.* **1953**, *21*, 836.

[15] A. Raja, A. Montoya-Castillo, J. Zultak, X.-X. Zhang, Z. Ye, C. Roquelet, D. a Chenet, A. M. van der Zande, P. Huang, S. Jockusch, J. C. Hone, D. R. Reichman, L. E. Brus, T. F. Heinz, *Nano Lett.* **2016**, *16*, 2328

[16] P. L. Hernández-Martínez, A. O. Govorov, H. V. Demir, *J. Phys. Chem. C* **2013**, *117*, 10203.

[17] G. P. Murphy, J. J. Gough, L. J. Higgins, V. D. Karanikolas, K. M. Wilson, J. A. Garcia Coindreau, V. Z. Zubialevich, P. J. Parbrook, A. L. Bradley, *Nanotechnology* **2017**, *28*, 115401.

[18] K. M. Goodfellow, C. Chakraborty, K. Sowers, P. Waduge, M. Wanunu, T. Krauss, K. Driscoll, A. N. Vamivakas, *Appl. Phys. Lett.* **2016**, *108*, 21101.

[19] J. R. Lakowicz, *Principles of Fluorescence Spectroscopy*; Lakowicz, J. R., Ed.; Springer US: Boston, MA, 2006.

[20] B. W. van der Meer, *FRET - Forster Resonance Energy Transfer*; Medintz, I.; Hildebrandt, N., Eds.; Wiley-VCH Verlag GmbH & Co. KGaA: Weinheim, Germany, 2013.

[21] D. Prasai, A. R. Klots, A. K. M. Newaz, J. S. Niezgoda, N. J. Orfield, C. A. Escobar, A. Wynn, A. Efimov, G. K. Jennings, S. J. Rosenthal, K. I. Bolotin, *Nano Lett.* **2015**, *15*, 4374.

[22] F. Prins, A. J. Goodman, W. A. Tisdale, *Nano Lett.* **2014**, *14*, 6087.

[23] S. Sampat, T. Guo, K. Zhang, J. A. Robinson, Y. Ghosh, K. P. Acharya, H. Htoon, J. A. Hollingsworth, Y. N. Gartstein, A. V. Malko, *ACS Photonics* **2016**, *3*, 708.

[24] Z. Chen, S. Berciaud, C. Nuckolls, T. F. Heinz and L. E. Brus, *ACS Nano* **2010**, *4*, 2964.

[25] G. Konstantatos, M. Badioli, L. Gaudreau, J. Osmond, M. Bernechea, F. P. Garcia de

Arquer, F. Gatti, F. H. L. Koppens, *Nat. Nanotechnol.* **2012**, *7*, 363.

[26] P. V. Kamat, *J. Phys. Chem. C* **2008**, *112*, 18737.

[27] M. Achermann, M. A. Petruska, D. D. Koleske, M. H. Crawford, V. I. Klimov, *Nano Lett.* **2006**, *6*, 1396.

[28] A. R. Clapp, I. L. Medintz, H. Mattoussi, *ChemPhysChem* **2006**, *7*, 47.

[29] U. Resch-Genger, M. Grabolle, S. Cavaliere-Jaricot, R. Nitschke, T. Nann, *Nat. Methods* **2008**, *5*, 763.

[30] H. Li, Q. Zhang, C. C. R. Yap, B. K. Tay, T. H. T. Edwin, A. Olivier, D. Baillargeat, *Adv. Funct. Mater.* **2012**, *22*, 1385.

[31] C. Lee, H. Yan, L. E. Brus, T. F. Heinz, J. Hone, S. Ryu, *ACS Nano* **2010**, *4*, 2695.

[32] V. K. Sangwan, D. Jariwala, I. S. Kim, K.-S. Chen, T. J. Marks, L. J. Lauhon, M. C. Hersam, *Nat. Nanotechnol.* **2015**, *10*, 403.

[33] C. C. Wu, D. Jariwala, V. K. Sangwan, T. J. Marks, M. C. Hersam, L. J. Lauhon, *J. Phys. Chem. Lett.* **2013**, *4*, 2508.

[34] N. Perea-López, Z. Lin, N. R. Pradhan, A. Iñiguez-Rábago, A. Laura Elías, A. McCreary, J. Lou, P. M. Ajayan, H. Terrones, L. Balicas, M. Terrones, *2D Mater.* **2014**, *1*, 11004.

[35] V. Klee, E. Preciado, D. Barroso, A. E. Nguyen, C. Lee, K. J. Erickson, M. Triplett, B. Davis, I. Lu, S. Bobek, J. McKinley, J. P. Martinez, J. Mann, A. A. Talin, L. Bartels, F. Léonard, *Nano Lett.* **2015**, *15*, 2612.

[36] R. H. Bube, *J. Appl. Phys.* **1993**, *74*, 5138.

[37] W. Zhou, X. Zou, S. Najmaei, Z. Liu, Y. Shi, J. Kong, J. Lou, P. M. Ajayan, B. I. Yakobson, J.-C. Idrobo, *Nano Lett.* **2013**, *13*, 2615.

[38] S. Tongay, J. Suh, C. Ataca, W. Fan, A. Luce, J. S. Kang, J. Liu, C. Ko, R. Raghunathanan, J. Zhou, F. Ogletree, J. Li, J. C. Grossman, J. Wu, *Sci. Rep.* **2013**, *3*, 2657.

[39] M. V. Bollinger, J. V. Lauritsen, K. W. Jacobsen, J. K. Nørskov, S. Helveg, F.

Besenbacher, *Phys. Rev. Lett.* **2001**, *87*, 196803.

[40] J. Zhang, H. Yu, W. Chen, X. Tian, D. Liu, M. Cheng, G. Xie, W. Yang, R. Yang, X. Bai, D. Shi, G. Zhang, *ACS Nano* **2014**, *8*, 6024.

[41] A. M. van der Zande, P. Y. Huang, D. A. Chenet, T. C. Berkelbach, Y. You, G. Lee, T. F. Heinz, D. R. Reichman, D. A. Muller, J. C. Hone, *Nat. Mater.* **2013**, *12*, 554.

[42] Y. Yu, C. Li, Y. Liu, L. Su, Y. Zhang, L. Cao, *Sci. Rep.* **2013**, *3*, 1.

[43] J.-H. Hur, J. Park, S. Jeon, *J. Phys. D. Appl. Phys.* **2017**, *50*, 65105.

[44] D. Hanlon, C. Backes, T. M. Higgins, M. Hughes, A. O'Neill, P. King, N. McEvoy, G. S. Duesberg, B. Mendoza Sanchez, H. Pettersson, V. Nicolosi, J. N. Coleman, *Chem. Mater.* **2014**, *26*, 1751.

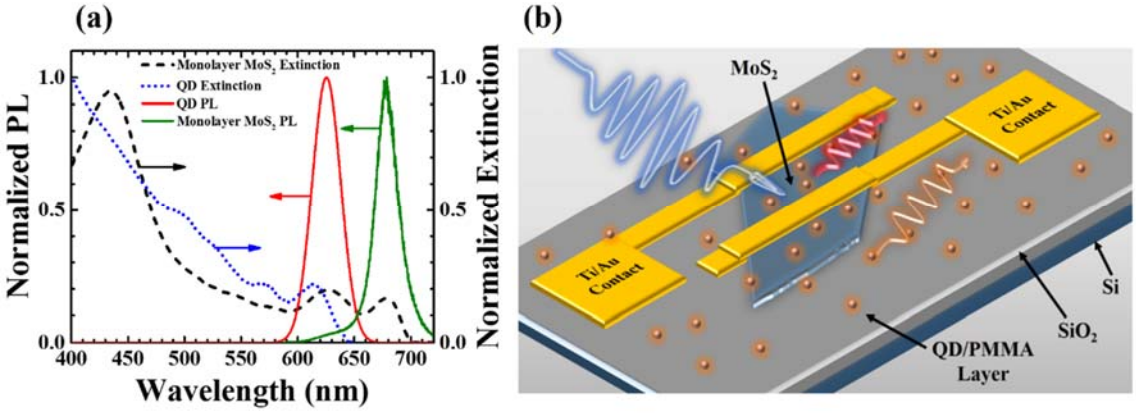

Figure 1. (a) Extinction spectra of monolayer MoS_2 (black dash) and QDs in PMMA (blue dot), and normalized PL spectra of monolayer MoS_2 (green solid) and QDs in PMMA (red solid). The PL spectra were acquired under excitation with a 405 nm pulsed laser diode. The extinction spectrum of monolayer MoS_2 was measured from a CVD-grown triangular monolayer on a quartz substrate. The extinction spectrum of the QDs was obtained from the solution of QDs in PMMA that was subsequently spincast onto the devices. (b) Schematic diagram of experimental device.

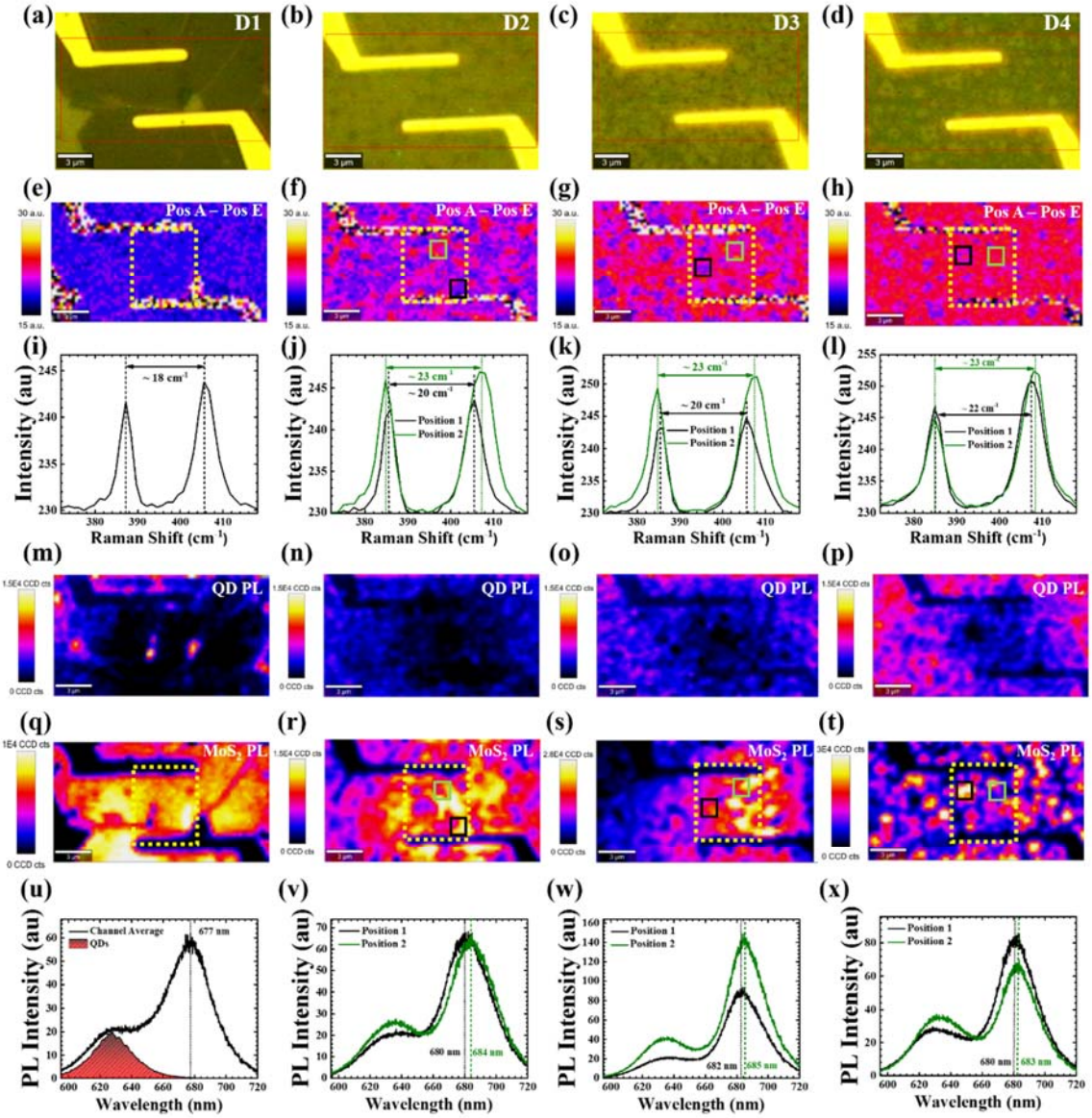

Figure 2. (a-d) Optical images of MoS_2 devices (red boxes indicate the PL and Raman mapping areas). (e-h) Raman maps indicating the separation between the *A* and *E* peak positions. Yellow dash box represents the channel in the devices. Black and green boxes correspond to the regions where the Raman and PL spectra were extracted, shown in (i-l) and (u-x), respectively. (m-p) PL maps of the same areas highlighted in the red boxes in the optical images (a-d).The PL maps are centered on the QD peak emission wavelength (630 nm). The maps clearly show that the QD emission is quenched most strongly on the monolayer device and less quenched moving to the right. (q-t) PL maps of the devices centered on the MoS_2 peak emission wavelength. (u-x) PL spectra extracted from the maps in areas indicated by black and green boxes on the Raman

maps in (f-h). The QD PL spectrum, measured from a position on the sample containing no MoS_2, is shown in (u) to indicate the peak position of the QDs relative to the MoS_2 B emission peak. There is a clear redshift in the MoS_2 peak emission wavelength as the MoS_2 thickness increases from monolayer to bilayer. The regions where there are a change in layer thickness are indicated by black and green boxes in the Raman maps and represented by the corresponding colors in the Raman and PL spectra in (i-l) and (u-x), respectively. Higher QD PL emission is observed on the regions of increased layer thicknesses, indicating a reduction in the NRET efficiency. The NRET efficiency is highest to the monolayer MoS_2. A full set of data for a bulk-like device is shown in Figure S3 (Supporting Information).

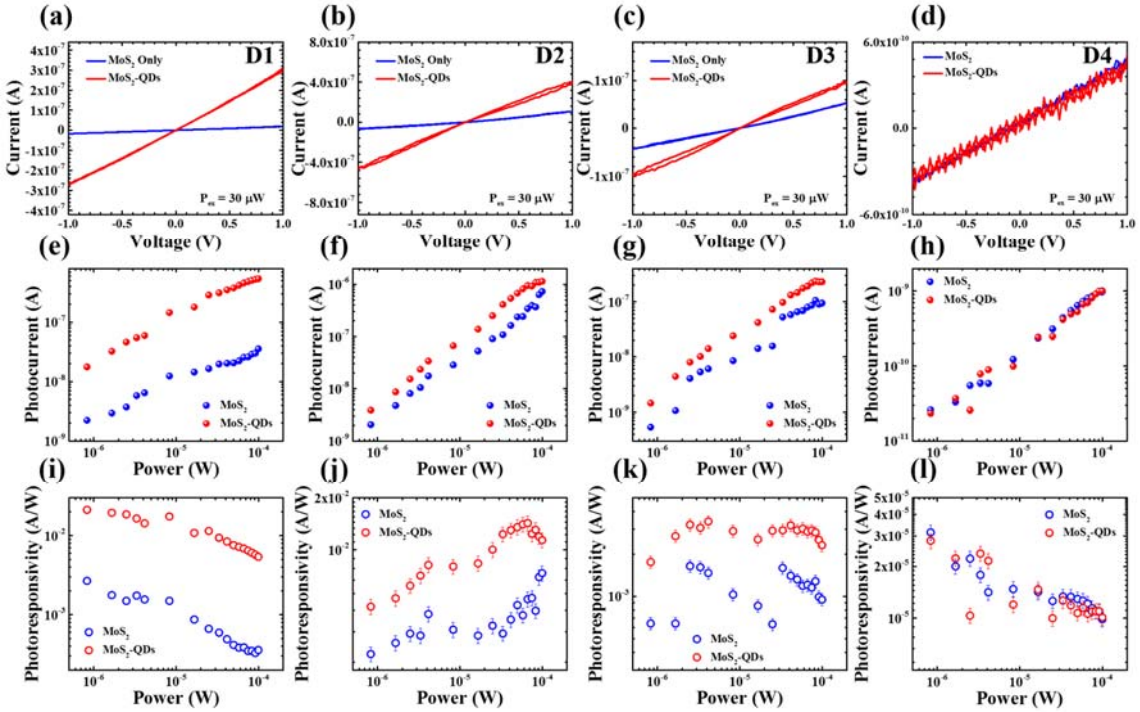

Figure 3. (a-d) I-V curves for the MoS_2 devices before (blue line) and after the addition of the QD sensitizing layer (red line). The I-V curves were measured under excitation from a 405 nm laser at an excitation power of 30 μW. (e-h) Plots of photocurrent as a function of excitation power for each of the MoS_2 device before (blue dots) and after the addition of the QD sensitizing layer (red dots). (i-l) Photoresponsivity of each device before (blue open circles) and after the addition of the QD sensitizing layer (red open circles).

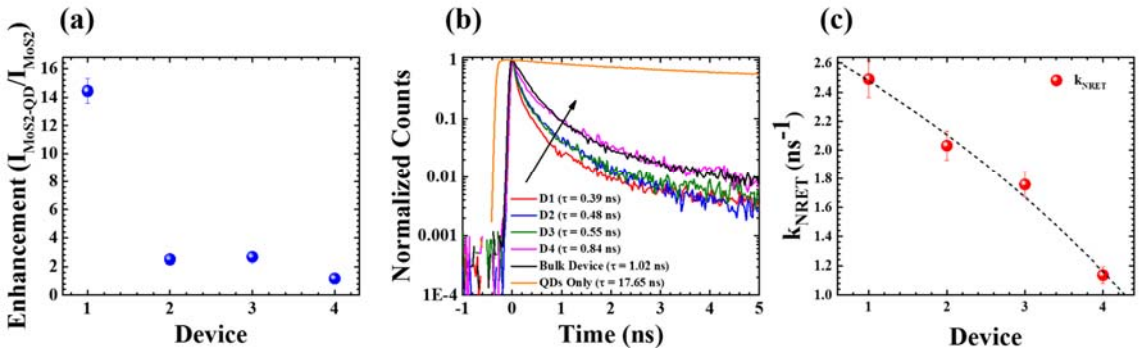

Figure 4. (a) Average photocurrent enhancement for each device. (b) PL decay curves of the QDs only (orange) and the QDs on each of the devices. The decays are presented over the first 5 ns for easier comparison of the curves. Full decays are presented in the supporting information, Figure S4. (c) NRET rate between the QDs and MoS_2 in each of the devices. The black dash line in c is a guide to the eye.

Table of contents entry:

This work demonstrates the importance of crystalline monolayers in quantum dot sensitized MoS_2 devices. Nonradiative energy transfer from semiconductor nanocrystal quantum dots to a variety of MoS_2 devices is studied. The MoS_2 devices consist of varying layer thickness and crystalline properties, including pristine monolayers, mixed monolayer/bilayer, polycrystalline bilayers, and bulk-like thicknesses. Large photocurrent enhancements require crystalline MoS_2 monolayers.

Keyword: monolayers, quantum dots, photonics, electro-optical devices

John J. Gough, Niall McEvoy, Maria O'Brien, Alan P. Bell, David McCloskey, John B. Boland,

*Jonathan N. Coleman, Georg S. Duesberg and A. Louise Bradley**

Title: Dependence of Photocurrent Enhancements in QD-Sensitized MoS_2 Devices on MoS_2 Film Properties

ToC figure

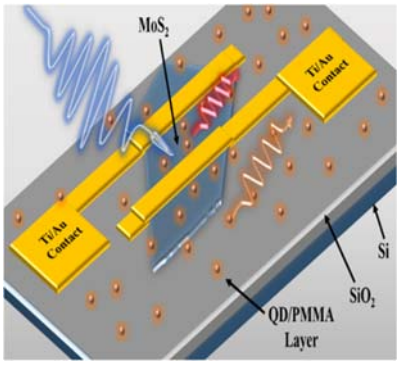

Supporting Information

Title: Dependence of Photocurrent Enhancements in QD-Sensitized MoS_2 Devices on MoS_2 Film Properties

*John J. Gough, Niall McEvoy, Maria O'Brien, Alan P. Bell, David McCloskey, John B. Boland, Jonathan N. Coleman, Georg S. Duesberg and A. Louise Bradley**

S1: Size distribution of quantum dots (QDs).

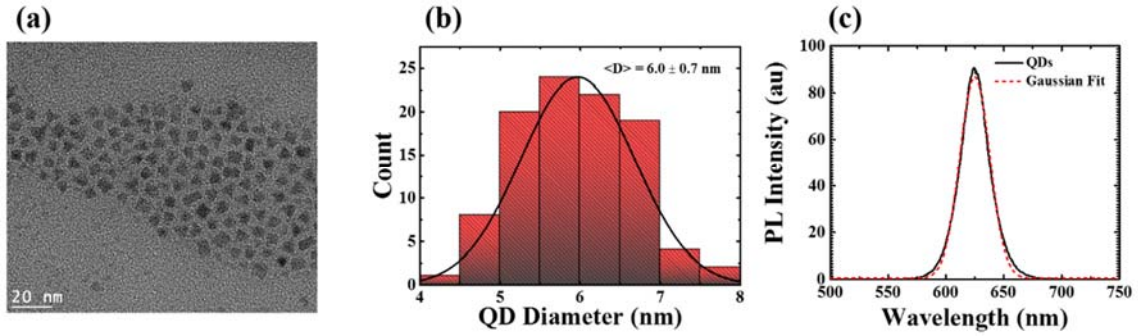

Figure S1: (a) TEM image of CdSeS/ZnS QDs. (b) Size distribution histogram of CdSeS/ZnS QD diameters. (c) PL spectrum of CdSeS/ZnS QDs in toluene (black solid) and Gaussian fit (red dash).

Figure S1a shows a typical TEM image of the alloyed CdSeS/ZnS QDs and a narrow QD size distribution of (6.0 ± 0.7) nm can be seen from the histogram in Figure S1b. Figure S1c shows the PL spectrum of the QDs in solution and a Gaussian fit to the spectrum. The full-width at half-maximum (FWHM) is (30.6 ± 0.1) nm further verifying the narrow size distribution of the QDs in the ensemble.

S2. Time-resolved and Spectral Photoluminescence (PL) Measurements of QDs on monolayer MoS_2.

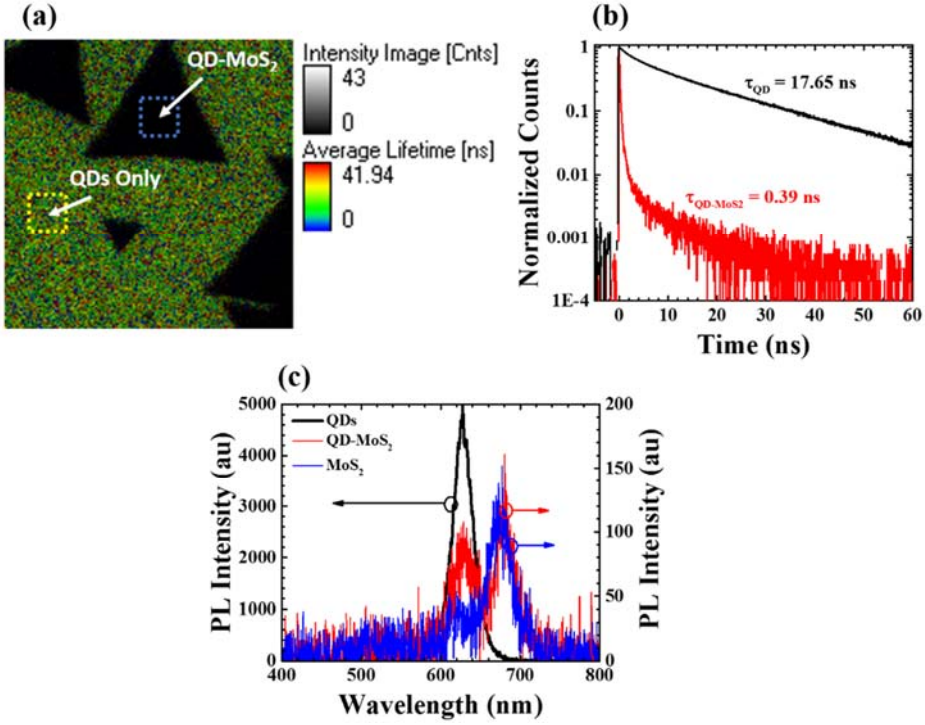

Figure S2: (a) Fluorescence lifetime map (80 μm x 80 μm) of QD film on a chip showing monolayer MoS_2 triangular flakes. (b) PL decays of QDs off the flake (black) and on monolayer MoS_2 device D1 (red). (c) PL spectra of QDs off the flake (black), QDs on monolayer MoS_2 (red) and MoS_2 before adding QDs (blue).

The quenching of the QD PL intensity and the lifetime is clear from the black triangles in the fluorescence lifetime map in Figure S2a. The reference QD PL spectrum and PL decay is measured ~ 20 μm away from the MoS_2 flake on the same chip as indicated in the dashed boxes in the example shown in Figure S2a. The PL decays and PL spectra shown in Figure S2b and Figure S2c, respectively, are averaged over 3 μm x 3 μm areas.The NRET efficiency, η_{NRET}, was calculated from the QD lifetimes as

$$\eta_{NRET} = 1 - \frac{\tau_{QD-MoS_2}}{\tau_{QD}} \quad (1)$$

where τ_{QD} is the lifetime of the QDs alone and $\tau_{QD\text{-}MoS2}$ is the lifetime of the QDs on the MoS_2. From the values given in Figure S2b, the NRET efficiency on the monolayer device was ~98%. Figure S2c shows the PL spectra of the QDs alone (black), the MoS_2 alone (blue) and the QDs and MoS_2 together (red). It is evident from the PL spectra that there is no enhancement of the MoS_2 PL intensity following the addition of the QD sensitizing layer as the MoS_2 PL intensity remains the same while the QD PL intensity has been substantially quenched, similar to the QD lifetime in Figure S2b. The NRET efficiency can also be quantified using the integrated PL spectra, $\eta_{NRET\text{-}PL}$, given by

$$\eta_{NRET-PL} = 1 - \frac{I_{QD-MoS_2}}{I_{QD}} \quad (2)$$

where $I_{QD\text{-}MoS2}$ and I_{QD} are the integrated PL spectra of the QDs on the MoS_2 and the integrated PL spectra of the QDs alone, respectively. The NRET efficiency calculated from the integrated PL spectra is ~99% which is in good agreement with the NRET efficiency extracted from the lifetimes.

S3: Bulk-like device characteristics.

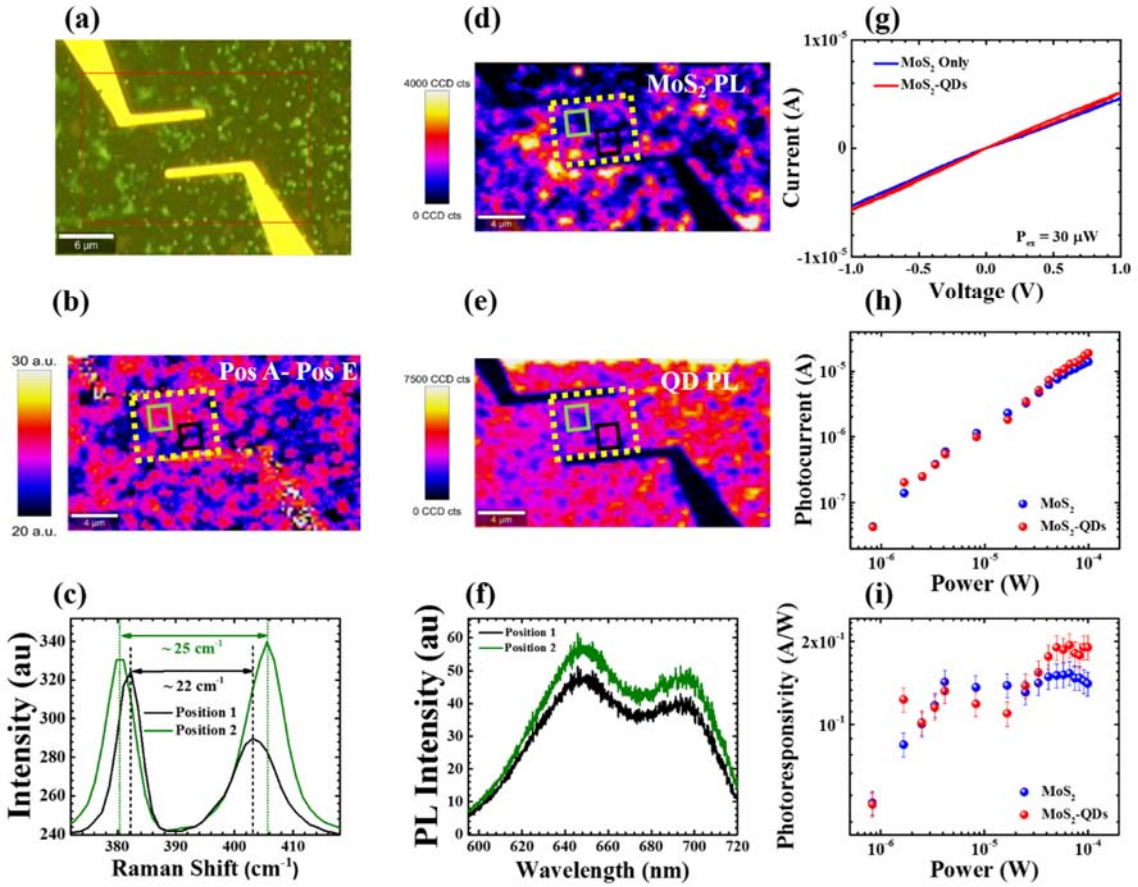

Figure S3: (a) Optical image of bulk-like device, D5. (b) Raman map of D5 plotting the separation between the *A* and *E* Raman peak positions. (c) Raman spectra corresponding to the positions labelled in black and green in (b). (d) PL map of D5 centred on the MoS_2 peak emission wavelength. (e) PL map of D5 centred on the QD peak emission wavelength. (f) PL spectra corresponding to the position labelled in black and green in (d) and (e). (g) I-V curve for device, D5, before (blue line) and after (red line) the addition of the QD sensitizing layer at a laser excitation power of 30 μW. (h) Plot of photocurrent vs. excitation power for device, D5, before (blue dot) and after (red dot) the addition of the QD sensitizing layer. (i) Photoresponsivity as a function of excitation power for device, D5, before (blue dots) and after (red dots) the addition of the QD sensitizing layer.

Similar to the polycrystalline bilayer device, D4, in the main manuscript there is little to no change in the electrical performance of the device after the addition of the QD sensitizing layer (Figure S3, panels g, h and i) indicating that the enhancement of the electrical properties of the devices through NRET from QDs in a sensitizing layer relies on the underlying crystallinity of the MoS_2 in the device channel. While this device consists mainly of multilayer/bulk-like thicknesses of MoS_2 there are some regions of the device that consist of bilayer MoS_2 as can be seen in blue in the Raman map (Figure S3b) and the corresponding Raman spectra for these regions is shown in black in Figure S3c. This bulk-like device gave the highest photocurrent and photoresponsivity values compared to all the monolayer/bilayer devices measured in this study.

S4: NRET efficiencies for all devices.

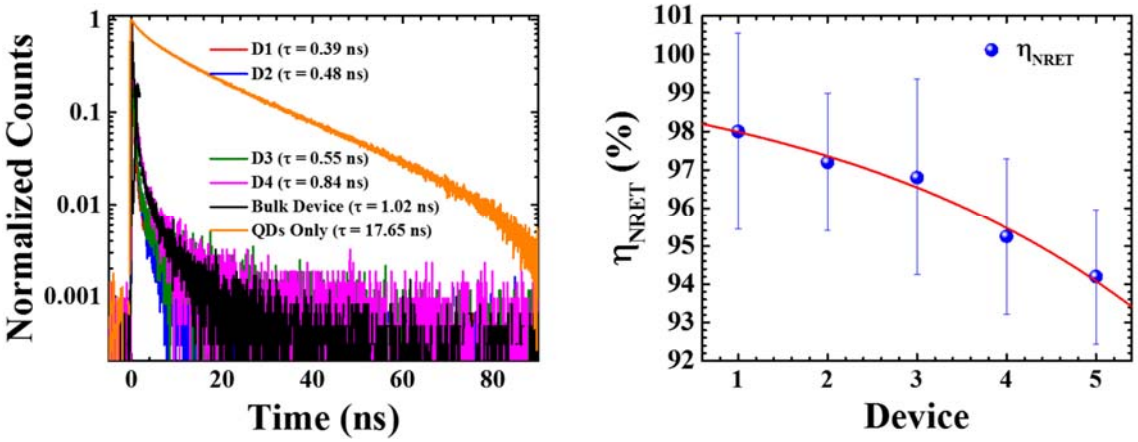

Figure S4: (a) Full PL decay curves of the QDs only (orange) and the QDs on each of the devices. (b) Plot of NRET efficiency, η_{NRET}, for each of the devices. Device 5 is the bulk like device shown in Figure S3.

Full decays of the QDs alone and on each of the MoS_2 devices are shown in Figure S4a. Figure S4b demonstrates how the NRET efficiency decreases as the devices become more polycrystalline resulting from larger portions of the device channel being occupied by bilayer MoS_2. The red line in the plot is a single exponential fit and is presented solely as a guide to the eye. Despite the fact that the NRET efficiency is decreasing as the device becomes more polycrystalline, the NRET process in this system is highly efficient with values >90% across all devices.

S5. Atomic Force Microscopy (AFM) profiles of QD/PMMA sensitizing layer.

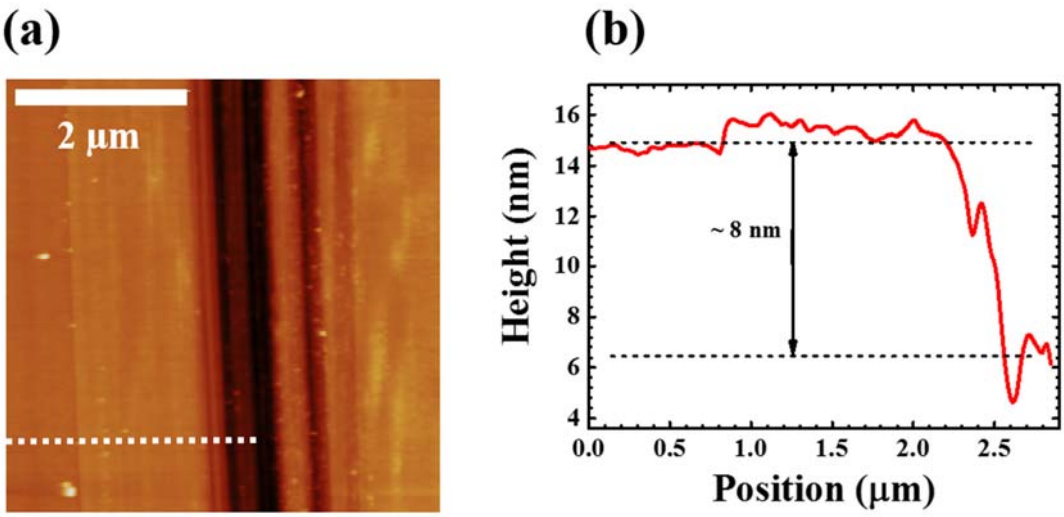

Figure S5: (a) AFM image of QD/PMMA film. (b) Height profile measured from the QD/PMMA film in (a). The dashed white line in (a) represents the position of the height profile presented in (b).

Figure S5a shows the AFM image of the QD/PMMA film with the corresponding height profile given in Figure S5b. A razor blade was used to score a single narrow trench in the QD/PMMA film and allow for the measurement of the film thickness.